https://doi.org/10.1016/j.apcatb.2020.119624

Highly Promoted Hydrogen Production Enabled by Interfacial P–N Chemical Bonds in Copper Phosphosulfide Z-Scheme Composite

Xiandi Zhang,[1,†] *Jia Yan,*[1,†] *and Lawrence Yoon Suk Lee*[1,2,*]

[1] Department of Applied Biology and Chemical Technology and the State Key Laboratory of Chemical Biology and Drug Discovery, The Hong Kong Polytechnic University, Hung Hom, Kowloon, Hong Kong SAR, China

[2] Research Institute for Smart Energy, The Hong Kong Polytechnic University, Hung Hom, Kowloon, Hong Kong SAR, China

[†] These authors equally contributed to this work.

*E-mail: lawrence.ys.lee@polyu.edu.hk (L. Y. S. Lee)

KEYWORDS: copper phosphosulfide; photocatalysis; hydrogen evolution reaction; interfacial charge transfer; P–N bond

Highlights

- A new Z-scheme composite consisting copper phosphosulfide ($Cu_3P|S$) and graphene-like C_3N_4 (GL-C_3N_4) was formed by interface engineering.
- $Cu_3P|S$/GL-C_3N_4 shows impressive photocatalytic H_2 generation rates (20.22 and 8.78 mmol g^{-1} h^{-1} with and without 0.5 wt.% Pt) and good durability.
- The P–N chemical bonds between $Cu_3P|S$ and GL-C_3N_4 serve as an interfacial charge transfer pathway across the Z-scheme junction.
- Abundant and active phosphosulfide structures preserved in the composite also contribute to high photocatalytic performance.

Graphical abstract

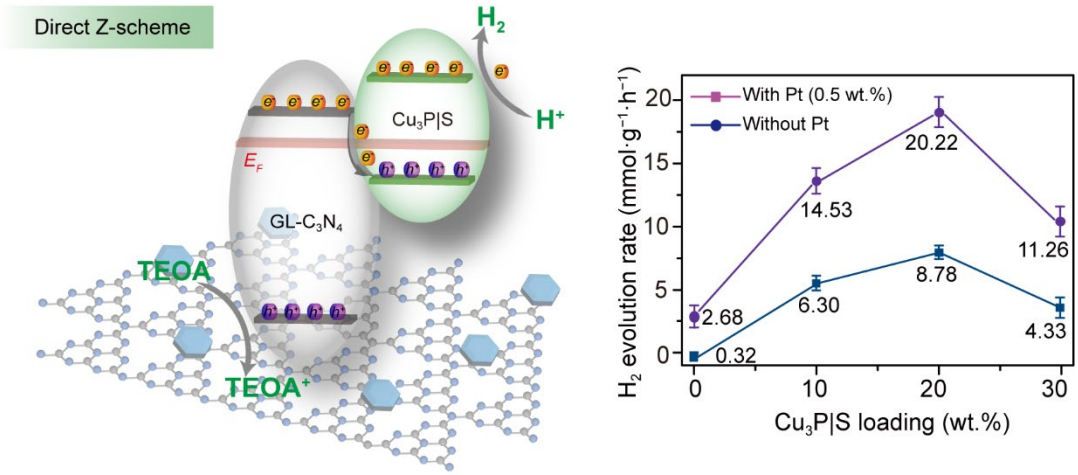

Abstract

Transition metal phosphosulfides (TMPSs) have shown great potential as efficient catalysts toward hydrogen evolution reaction (HER). To further understand and promote the catalytic activity at the phosphosulfide (PS) structures, the multifunctional role of TMPS needs to be explored. Herein, we report copper phosphosulfide ($Cu_3P|S$) coupled with graphene-like C_3N_4 (GL-C_3N_4) as an excellent HER photocatalyst with a hydrogen production rate of 8.78 mmol g^{-1} h^{-1} (20.22 mmol g^{-1} h^{-1} with 0.5 wt.% Pt). Systematic investigations on the interaction between $Cu_3P|S$ and GL-C_3N_4 unveil that such impressive photocatalytic activity arises from the interfacial P–N chemical bond that constructs a Z-scheme heterostructure. Time-resolved photoluminescence analysis indicates a considerably suppressed recombination rate of photoexcited charge carriers at the interface, which facilitates electron transfer and enhances the reducibility of electrons in the conduction band of $Cu_3P|S$. This work provides new design strategies for employing TMPSs as photocatalysts for highly efficient HER and other photoreduction reactions.

1. Introduction

Hydrogen, a zero-emission and recyclable energy carrier, has great potential to become an alternative to fossil fuels to relieve the global concerns on energy consumption and environmental degradation [1-3]. Among the currently available production methods, photocatalytic hydrogen evolution reaction (HER) provides the most eco-friendly and sustainable pathway [4, 5]. Despite the efforts devoted to the development of effective photocatalysts [6-9], the practical application of photocatalytic HER is largely hampered by insufficient light utilization and fast recombination of photogenerated electron–hole pairs, leading to low energy conversion efficiencies. Finding a way to facilitate the charge carrier transfer in an effective photocatalytic system is one of the keys to accomplish high hydrogen production rates.

Transition metal phosphosulfides (TMPSs) have recently attracted great attention because of their excellent catalytic performances toward reduction reactions [10-16]. Having a unique phosphosulfide (PS) structure, they exhibit excellent catalytic activity and stability superior to the corresponding phosphides and sulfides particularly for the production of (photo)electrochemical hydrogen. Both experimental and theoretical results suggest that the PS structure can provide optimized proton adsorption/desorption energies to boost the HER catalytic performance [10, 11]. Recently, we reported a new copper phosphosulfide ($Cu_3P|S$) as the first PS structure-based active HER photocatalyst [16]. The PS structure in $Cu_3P|S$ lowers the Gibbs free energy (ΔG_{H*}) of adsorption for atomic hydrogen and increases the number of active sites, leading to the promotion of the photocatalytic activity, but its energy conversion efficiency is still limited by the fast recombination of electron–hole pairs.

In general, modulating the charge transfer route in a photocatalytic system can effectively lead to higher catalytic activity by preventing the recombination of photogenerated electron–hole pairs [17]. In this aspect, direct Z-scheme and S-scheme heterostructures with a specific charge transfer

route between two semiconductors have been proposed not only for suppressing the recombination of charge carriers but also for accelerating electron transfer rate to preserve the strong redox power [18-21]. The enhanced photocatalytic activity arising from the highly efficient charge carrier separation in Z-scheme or S-scheme systems has been demonstrated in many studies [21], but less attention has been paid to the effect of the interface formed between the two semiconductors. The interface between two components dictates the efficiencies of charge transfer and separation in hybrid structures, and thus is the key factor in preventing the charge recombination. At the interface of Z-scheme system, electrons and holes can be spatially separated toward different components, largely reducing the charge recombination rate in bare components [21, 22]. The interface parameters, such as interfacial compositions, areas, facets, electronic coupling, and band bending, all greatly influence the charge transfer and separation efficiency. In particular, the chemical environment at such interfaces is crucial to the promoting of charge transfer at the atomic level. The influence of chemical bonds formed by interfacial engineering has been recently recognized as having a positive effect on the photocatalytic process by steering and facilitating the charge flow between two components, for examples, the C–N–Br bond in $CsPbBr_3$/g-C_3N_4 [23] and Co–P bond in Co_2P/black phosphorus [22].

In this work, we constructed a direct Z-scheme system by coupling the Cu_3P|S nanoplates with graphene-like C_3N_4 (GL-C_3N_4) nanosheets *via* interface engineering, to explore its application toward photocatalytic HER. Thermally exfoliated from g-C_3N_4, the GL-C_3N_4 has a thin-layer structure of *ca*. 2-3 nm thickness that offers a large surface area and abundant functional groups for chemical interaction with Cu_3P|S [24, 25]. Under simulated sunlight, the Cu_3P|S/GL-C_3N_4 composite achieved an extraordinary H_2 production rate of *ca*. 9 mmol g^{-1} h^{-1} (*ca*. 20 mmol g^{-1} h^{-1} with only 0.5 wt.% Pt) with good durability, a rate that marks one of the highest HER rates reported so far. By systematically investigating the interaction between Cu_3P|S and GL-C_3N_4, such highly enhanced

HER activity of $Cu_3P|S/GL\text{-}C_3N_4$ is demonstrated with the intimate contact *via* P–N chemical bond at the interface, and the photocatalytic mechanism has been proposed.

2. Experimental section

2.1. Materials and chemicals

Copper (I) chloride (CuCl, 97%), oleylamine (70%), trioctylphosphine (97%), trioctylphosphine oxide (90%), sodium hypophosphite monohydrate ($NaH_2PO_2 \cdot H_2O$, 99%), *o*-dichlorobenzene (99%), triethanolamine (TEOA, 99%), 5,5-dimethyl-1-pyrroline-*N*-oxide (DMPO, 97%), chloroplatinic acid hydrate ($H_2PtCl_6 \cdot xH_2O$, ≥99.9%) and Nafion (5 wt.%) were purchased from Sigma Aldrich. Sulfur powder (99.98%) was purchased from Arcos. All chemicals were used as received.

2.2. Synthesis of Cu_3P and $Cu_3P|S$ nanoplates

The Cu_3P nanoplates were synthesized following the procedure in our previous report [16]. Briefly, CuCl (1 mmol) and trioctylphosphine oxide (2.58 mmol) were dissolved in 10 mL oleylamine and heated to 100 °C in N_2 atmosphere for 30 min. To this mixture was injected trioctylphosphine (1.12 mL) at 150 °C under vigorous stirring. After about 5 min reaction, the reaction mixture was then purged with PH_3 gas at 230 °C. After 20 min of reaction, the temperature was lowered and kept at 200 °C for 15 min. The reaction solution was cooled down to ambient temperature, and the product was collected by centrifugation, followed by washing with acetone three times. $Cu_3P|S$ nanoplates were prepared with a similar procedure with the addition of elemental sulfur (1 mmol) dissolved in 1 mL *o*-dichlorobenzene after the purging with PH_3 gas.

2.3. Synthesis of graphene-like C_3N_4 ($GL\text{-}C_3N_4$)

The graphene-like C_3N_4 ($GL\text{-}C_3N_4$) was synthesized in a muffle furnace using melamine as a precursor. Briefly, melamine (2 g) was calcined at 550 °C for 4 h at a heating rate of 2 °C min^{-1}. The

as-synthesized bulk graphitic C_3N_4 (g-C_3N_4, 0.5 g) was further calcined at 550 °C for 1 h with a ramping rate of 5 °C min^{-1}. After cooling to room temperature, the sample was re-heated at 550 °C for another hour with a ramping rate of 2 °C min^{-1} to yield GL-C_3N_4 as white powders.

2.4. Synthesis of Cu_3P/CN and Cu_3P|S/CN composites

The as-synthesized Cu_3P or Cu_3P|S (4 mg) was dispersed in hexane (10 mL) by sonicating for 30 min. GL-C_3N_4 (40 mg) was also dispersed in hexane (20 mL) separately by sonicating for 30 min and added to the Cu_3P or Cu_3P|S suspension, followed by sonication for another 90 min. The composite product GL-C_3N_4/Cu_3P (Cu_3P/CN) or GL-C_3N_4/Cu_3P|S (Cu_3P|S/CN) was obtained after centrifugation at 9,000 rpm for 5 min, followed by drying under vacuum overnight. For comparison, a control sample was prepared by physically mixing Cu_3P|S (10 wt.%) and GL-C_3N_4 (denoted as p-Cu_3P|S/CN), which were separately sonicated in hexane for 2 hours, followed by drying in the vacuum oven. For charge flow tracking, Pt nanoparticles were photodeposited onto Cu_3P|S/CN by adding H_2PtCl_6 (0.5 wt.%) to the photoreaction suspension of Cu_3P|S/CN and irradiated with a solar simulator (Ceaulight, 450 W, 1 sun) equipped with an AM 1.5 air mass filter for 2 hours. The Pt-deposited Cu_3P|S/CN was collected by centrifugation, washed with DI water three times, and dried in a vacuum oven.

2.5. Material Characterization

Transmission electron microscopic (TEM) images and elemental distribution data were obtained using a JEOL JEM-2100F STEM equipped with an energy dispersive spectrometer (EDS) operating at 200 kV. The as-prepared samples were dispersed in chloroform and drop-cast onto a holey carbon-coated 400 mesh Ni TEM grid. Rigaku SmartLab X-ray diffractometer with Cu Kα radiation was employed to record powder X-ray diffraction (XRD) patterns in the 2θ range between 20° and 70° with a step size of 0.02°. UV-Vis diffuse reflectance spectra were measured using a Cary 4000 UV-

Vis spectrophotometer. X-ray photoelectron spectroscopy (XPS) was carried out with an X-ray photoelectron spectrometer (ESCALAB 250Xi, Thermo Fisher) with a monochromic Al Kα X-ray source and a pass energy of 1486.6 eV. The data were analyzed using CasaXPS software with a background type of Shirley and peak profile of Gaussian-Lorentzian GL(30). The electron spin resonance (ESR) analysis was conducted on a Bruker model ESR JES-FA200 spectrometer using the spin-trapping reagent DMPO. Photoluminescence (PL) spectra were measured on a FLS1000 fluorescence spectrophotometer (Edinburgh Instruments Ltd.) with an excitation wavelength of 325 nm. Time-resolved PL decay curves were recorded on the same spectrophotometer with a 375 nm pulsed laser. The obtained decay curves were fitted based on the bi-exponential kinetic function:

$$I(t) = A_1 \exp(-t/\tau_1) + A_2 \exp(-t/\tau_2)$$

where A_1 and A_2 are the corresponding amplitudes and τ_1 and τ_2 are the emission lifetimes. The Chi-square, χ^2 was kept between 1 and 1.3 for all the fitted curves. The electron transfer rate k_{ET} of composite was calculated based on $k_{ET} = 1/\tau_{ave}(Cu_3P|S/CN) - 1/\tau_{ave}(GL\text{-}C_3N_4)$ [26-28].

2.6. Electrochemical measurements

The as-prepared sample (3 mg) was dispersed in a mixed solution of deionized water (480 μL), ethanol (480 μL), and Nafion (40 μL, 5 wt.%, Sigma-Aldrich) and sonicated for 30 min. This catalyst ink (100 μL) was drop-cast onto a carbon fiber paper (1 × 1 cm^2) and used as the working electrode. Electrochemical measurements were conducted in a three-electrode system with a saturated calomel electrode (SCE) and graphite used as the reference and counter electrodes, respectively, in phosphate buffer (pH = 7.4) using a CHI 700E electrochemical station. Mott-Schottky plot was constructed based on the electrochemical measurements as follows: The as-prepared catalyst ink (10 μL) was deposited onto a glassy carbon electrode (GCE) and used as the working electrode. The required data were collected by measuring the space charge layer capacitance over a scanned range of applied

potentials (–1.0 to 1.0 V) at 1,000 Hz.

2.7. Photocatalytic hydrogen generation reaction

The as-prepared catalyst (3 mg) was dispersed in the solvent containing deionized water (17 mL) and TEOA (3 mL) and bubbled with Ar for 30 min. The solution was then irradiated with a solar simulator (Ceaulight, 450 W, 1 sun) equipped with an AM 1.5 air mass filter. The reaction product was periodically sampled from the headspace and analyzed by an Agilent 7890 B gas chromatograph equipped with a thermal conductivity detector using N_2 as the carrier gas. The apparent quantum efficiency (AQE) for hydrogen production was measured using a 300 W Xe lamp with a filter (λ = 400 nm) and calculated based on the following equation:

$$\text{AQE (\%)} = \frac{2 \times \text{amount of hydrogen produced}}{\text{number of incident photons}} \times 100$$

3. Results and discussion

The copper phosphide (Cu_3P) nanoplates are prepared *via* a wet chemical method in which a Cu-oleylamine complex is reacted with PH_3 gas (**Scheme 1**). A similar reaction in the presence of elemental S (33.3 mol% of P) yields the copper phosphosulfide ($Cu_3P|S$) nanoplates with homogeneous S doping of 26.8%, as verified by an energy dispersive spectrum (EDS, **Table S1** in the supporting Information). According to our previous study, the introduction of S during Cu_3P synthesis partially replaces the original P atoms without disrupting the initial Cu_3P crystal structure [16]. This replacement of P by S induces the formation of Cu-S bonds in Cu_3P crystal lattice, creating homogeneous phosphosulfide (PS) structures, as shown in the characterization section. These as-prepared Cu_3P and $Cu_3P|S$ nanoplates are then combined with graphene-like C_3N_4 (GL-C_3N_4) by

sonication in hexane to form Cu_3P/GL-C_3N_4 (Cu_3P/CN) and Cu_3P|S/GL-C_3N_4 (Cu_3P|S/CN) nanocomposites, respectively (for details, see Experimental section).

3.1. Characterization of Cu_3P|S/GL-C_3N_4 composite

The morphology of the as-prepared samples was first investigated by transmission electron microscopy (TEM). **Figure 1a** shows regular hexagonal Cu_3P nanoplates with an average edge length of *ca*. 75 nm. With the incorporation of S, some nanoplates change to irregular-shaped nanoplates with blunt edges, due to the larger atomic size of S [16] (**Figure 1b**). The TEM image of GL-C_3N_4 in **Figure S1a** displays a typical two-dimensional (2D) nanosheet morphology with a wrinkled surface. The sonication of Cu_3P (or Cu_3P|S) nanoplates together with the GL-C_3N_4 appear to anchor the nanoplates on the GL-C_3N_4 nanosheet, forming a Cu_3P/CN (or Cu_3P|S/CN) composite (**Figure 1c** and **d**). Most of the Cu_3P and Cu_3P|S nanoplates in these composites maintain their original shapes with a few of them exhibiting ill-defined edges, probably due to the prolonged sonication or possible chemical reaction between Cu_3P or Cu_3P|S and GL-C_3N_4. However, the unchanged *d*-spacing (2.02 Å for (300) planes) in the high-resolution TEM (HRTEM) images (insets in **Figure 1a-d**) indicates that the Cu_3P crystal structure is preserved after sulfurization and composite formation.

The unchanged crystal structure was also verified by comparing the X-ray diffraction (XRD) patterns (**Figure 1e**). The Cu_3P and Cu_3P|S nanoplates show a similar diffraction pattern, where the peaks observed at 36.1°, 39.2°, 41.8°, 45.1°, and 46.5° match well with the (112), (202), (211), (300), and (113) planes of Cu_3P (PDF# 02-1263) [29, 30], confirming that Cu_3P|S still retains the crystal structure of Cu_3P. The Cu_3P/CN and Cu_3P|S/CN composites also display all these peaks, as well as two additional peaks at 13.1° and 27.8°, which correspond to the characteristic (100) and (002) lattice planes of GL-C_3N_4 [31], verifying the coexistence of GL-C_3N_4 in the composites. The decreased

intensity of the Cu_3P and $Cu_3P|S$ peaks in the composites is due to the low loading amounts of Cu_3P and $Cu_3P|S$ nanocrystals (10 wt.%). The elemental mappings of $Cu_3P|S/CN$ (**Figure S1b**) display the even distribution of Cu, P, and S atoms in the region of hexagonal nanoplates and C and N signals in the matrix.

Understanding the nature of interactions between GL-C_3N_4 and $Cu_3P|S$ or Cu_3P is crucial to the modulation of the catalytic activity of the composites. Fourier-transform infrared spectroscopy (FTIR) was employed to investigate the chemical environment in the composites (**Figure 2a**). Both Cu_3P/CN and $Cu_3P|S/CN$ exhibit typical stretching and bending vibrations of GL-C_3N_4, featuring the characteristic peaks of triazine ring at 807 cm^{-1} and multiple peaks corresponding to the stretching modes of aromatic C–N and C=N bonds in the region of 1,200 – 1,650 cm^{-1} [24, 32]. In addition, the presence of abundant $–NH_x$ groups attached on the GL-C_3N_4 surface is suggested by the absorption band between 3,000 and 3,500 cm^{-1} [23]. It is worth noting that a new signal associated with the P–N breathing motion appears at 948 cm^{-1} in the spectra of both composites (right panel of **Figure 2a**) [30, 32], suggesting the successful coupling of Cu_3P and $Cu_3P|S$ with GL-C_3N_4 *via* P–N bonding. In addition, the relative intensity of the GL-C_3N_4-related peaks between 3,000 and 3,500 cm^{-1} has been reduced by 28.5 %, supporting the P–N chemical interactions between GL-C_3N_4 and Cu_3P or $Cu_3P|S$ [23].

The chemical interactions of Cu_3P and $Cu_3P|S$ with GL-C_3N_4 were further verified by X-ray photoelectron spectroscopy (XPS, **Figure 2b-f**). The XPS survey spectrum reveals the existence of C, N, Cu, P, and S in $Cu_3P|S/CN$ with no other elements present (**Figure S2**). In the C 1s region of high resolution XPS spectra, all the samples can be fitted to the three peaks at 284.8, 286.2, and 288.2 eV, which are attributed to C–C species from impurities, $C–NH_2$ in heptazine units, and N–C=N coordination in triazine rings of GL-C_3N_4, respectively (**Figure 2b**) [23]. The N 1s region of GL-C_3N_4 exhibits four typical peaks at 398.4, 399.2, 401.0, and 404.1 eV (**Figure 2c,** black line),

which are associated with sp^2-hybridized N (C–N=C) in triazine rings, tertiary N (N–$(C)_3$), NH_x from amino groups, and positive charge localization in heterocycles, respectively [23, 24]. Both Cu_3P/CN and Cu_3P|S/CN display similar N 1s spectra with four peaks (**Figure 2c,** light and dark blue lines). It should be noted that the peak for N in amino groups (–NH_x) shows a shift of 0.2 eV toward a lower binding energy upon the composite formation. Considering the peak positions other N are unchanged, such a negative shift suggests that the N atoms of surface amino groups in GL-C_3N_4 chemically interact with Cu_3P and Cu_3P|S [33]. A similar but opposite peak shift is observed in the P 2p region of Cu_3P/CN and Cu_3P|S/CN. The pristine Cu_3P and Cu_3P|S exhibit two peaks at 129.4 and 133.9 eV, corresponding to P^{3-} of Cu–P bond and P–O species due to surface oxidation, respectively [34]. The Cu-P peaks in Cu_3P/CN and Cu_3P|S/CN shift by 0.2 eV toward a higher binding energy while the P–O peaks remain at the same binding energy (**Figure 2d**). It can be inferred from such concomitant N 1s and P 2p peak shifting in the opposite direction that there are strong chemical bonding interactions (*i.e.*, P–N bonds) between P atoms of Cu_3P or Cu_3P|S and amino groups of GL-C_3N_4, a conclusion that is in a good agreement with the FTIR results [33, 35]. Meanwhile, the Cu 2p spectrum of Cu_3P|S displays two sets of Cu $2p_{3/2}$ and $2p_{1/2}$ peaks (**Figure 2e**), where the fitted peaks at 931.7 and 951.9 eV are attributed to the Cu^+ species in Cu_3P [36], while those at 933.7 and 953.1 eV are assigned to the Cu^{2+} species of Cu-S bond in the PS structure [16, 37]. Both sets of Cu^+ and Cu^{2+} peaks are also evident in the Cu_3P|S/CN composite, indicating the existence of Cu–S bond. This is also supported by the S 2p peaks at 161.4 and 163.0 eV that confirm the presence of the S^{2-} species (**Figure 2f**) and also assure the structural integrity of PS structure during the formation of the Cu_3P|S/CN composite [10]. No other peaks indicating the interaction of S with GL-C_3N_4 are observed, perhaps partially due to the small amount of S atoms in the composites.

3.2. Photocatalytic performance on hydrogen evolution

To understand how such hybridization of Cu_3P and $Cu_3P|S$ with GL-C_3N_4 *via* P–N bonds affects the photoreduction activity, a physical mixture of $Cu_3P|S$ and GL-C_3N_4 without chemical bonds was prepared as a control sample (denoted as p-$Cu_3P|S$/CN; see Experimental section for details). **Figure 3a** compares the photocatalytic activity of the samples toward hydrogen evolution reaction (HER), which was measured using 15 % TEOA as a sacrificial agent for three hours. Pristine Cu_3P and $Cu_3P|S$ nanoplates generate only trace amounts of H_2, while a similar H_2 production rate of 0.32 mmol g^{-1} h^{-1} is recorded with GL-C_3N_4 and p-$Cu_3P|S$/CN. Both Cu_3P/CN and $Cu_3P|S$/CN composites exhibit an impressive HER rate of 2.55 g^{-1} h^{-1} and 6.31 mmol g^{-1} h^{-1}, increased by nearly 8- and 20-fold from the bare GL-C_3N_4, respectively. The HER rate of standard catalyst TiO_2 Degussa P-25 (P25) measured under the same conditions for comparison is only 0.16 mmol g^{-1} h^{-1}. Meanwhile, no H_2 is detected in the control experiments performed under dark or without catalysts. The durability of $Cu_3P|S$/CN against photocorrosion is demonstrated by its maintaining such a remarkable HER rate for a continuous 24-hour reaction without any obvious loss of activity (**Figure 3b**). Its stability in long-term photoreduction is further confirmed by post-HER XRD and TEM characterizations of $Cu_3P|S$/CN by which disclose an unchanged crystal structure and morphology (**Figures 3c** and **S3**). The $Cu_3P|S$/CN composite can be optimized to deliver a HER rate of 8.78 mmol g^{-1} h^{-1} at 20 wt.% $Cu_3P|S$ loading with an apparent quantum efficiency of 7.10 % at monochromatic light of 400 nm. This HER rate is nearly 30 times higher than bare GL-C_3N_4, by modulating the loading quantity of $Cu_3P|S$ (**Figure 3d**). With the assistance of 0.5 wt.% Pt, the electron transfer and catalytic rates are further increased [38] and an impressive HER rate of 20.22 mmol g^{-1} h^{-1} has been achieved, which is the highest rate among the recently reported composites of metal phosphide or sulfide, C_3N_4 and other common photocatalysts (**Table S2**). However, further increasing the $Cu_3P|S$ loading to 30 wt.% leads to a decrease in HER rate (4.33 mmol g^{-1} h^{-1}), which might be caused by the inaccessible active sites or lower light absorption due to the aggregation of excessive $Cu_3P|S$

nanoplates [39, 40].

3.3. Mechanism of Photocatalysis

The highly promoted photocatalytic activity of Cu_3P|S/CN seems to originate from the PS structure and its P–N chemical bonding to GL-C_3N_4. To gain insight into such promotional effects, the optical properties of the composites were investigated. **Figure 4a** presents the light absorption and band edge determined by UV-Vis diffuse reflectance spectroscopy (DRS). The pristine GL-C_3N_4 exhibits a sharp absorption edge at *ca*. 430 nm and the corresponding Tauc plot indicates a band gap of 2.85 eV (**Figure S4**, top) [24]. On the other hand, consistent with previous reports, Cu_3P and Cu_3P|S show a broad absorption tail of up to 780 nm with no obvious absorption edges (**Figure 4a**, green lines) and a similar band gap of 1.52 eV is determined (**Figure S4**, bottom) [16, 36]. Once coupled with GL-C_3N_4, both Cu_3P/CN and Cu_3P|S/CN exhibit an absorption tail in the range of 450 to 700 nm with an absorption edge similar to that of GL-C_3N_4 (**Figure 4a**, blue lines). This implies that the composite formation with Cu_3P and Cu_3P|S contributes to the visible light absorption of GL-C_3N_4 without affecting the band gap [39].

The electronic structures of Cu_3P/CN and Cu_3P|S/CN were determined by collecting the valence band XPS (VB-XPS) spectra of GL-C_3N_4, Cu_3P, and Cu_3P|S as shown in **Figure 4b**. The VB positions of GL-C_3N_4, Cu_3P, and Cu_3P|S are estimated as 1.70, 0.77, and 0.77 V, respectively, against normal hydrogen electrode (NHE) at pH = 7 using the formula, $E_{NHE} = \Phi + 1.79$ (or 0.86) – 4.44 (E_{NHE}: potential of NHE; Φ of 4.35 eV: the electron work function of the analyzer) [39, 41, 42]. The formation of PS structure, consistent with our previous report, has no obvious influence on the band position [16]. Combining with the band gap (E_g) estimated by DRS spectra, the conduction bands (CB) of GL-C_3N_4 and Cu_3P|S are calculated as –1.15 and –0.75 V *vs.* NHE pH = 7, according to $E_{VB} = E_{CB} + E_g$ [36]. In addition, the positive slope of the Mott-Schottky plot (**Figure S5a**) indicates that

the GL-C_3N_4 is a typical *n*-type semiconductor whose estimated Fermi level (E_F) is close to the CB [39]. On the other hand, the $Cu_3P|S$ is a *p*-type semiconductor with a negative slope in the Mott-Schottky plot, exhibiting a lower E_F close to its VB [43]. To precisely determine the position of E_F, ultraviolet photoelectron spectroscopy (UPS) were engaged (**Figure S5b**). The work functions (Φ) of GL-C_3N_4 and $Cu_3P|S$ were estimated to be 4.13 and 5.30 eV (*vs*. vacuum), respectively, by using an equation, $h\nu$ (He, 21.22 eV) = E_{cutoff} + Φ, where E_{cutoff} represents the beginning of secondary photoemission [28]. Thus, the E_F of GL-C_3N_4 and $Cu_3P|S$ were calculated to be -0.72 and 0.45 eV *vs*. NHE at pH = 7. Based on this information, we constructed the band structures for GL-C_3N_4 and $Cu_3P|S$, as shown in **Figure 4c**.

When the $Cu_3P|S$ nanoplates are coupled with GL-C_3N_4 to form a heterojunction *via* P–N chemical interaction, the E_F values of the two components shift to -0.14 to match each other, based on the UPS measurement (**Figure S5b**, bottom), thus rearranging the band positions in $Cu_3P|S$/CN composite as shown in **Figure 4d** [36]. At such an interface of two dissimilar semiconductors, either *p-n* heterojunction or direct Z-scheme is possible, of which the main difference between the two lies in the charge transfer direction [44]. To confirm the proposed band positions of samples and verify the direction of interfacial charge flow in $Cu_3P|S$/CN, electron spin resonance (ESR) spectra were collected using spin-trapping agent DMPO. Under simulated sunlight, weak DMPO-•OH signals are observed from GL-C_3N_4, while no obvious peak is found in $Cu_3P|S$ (**Figure S6a**), in good agreement with the estimated E_{VB} positions. The DMPO-•OH signal is largely intensified in the spectra of $Cu_3P|S$/CN, which is a solid evidence of the accumulated holes in the VB that enhance the oxidation ability of GL-C_3N_4. Also, **Figure S6b** shows DMPO-•O_2^- signals from all three samples, which indicates their E_{CB} positions are more negative than $E(\bullet O_2^-/O_2)$ = −0.33 V (*vs*. NHE, pH = 7) as proposed in **Figure 4c** and **4d** [45]. In particular, $Cu_3P|S$/CN composite exhibits the highest peak intensity, indicating a stronger reduction ability than individual GL-C_3N_4 and $Cu_3P|S$ [46]. To

confirm the direction of charge flow, Pt nanoparticles were deposited on Cu_3P|S/CN by photoreduction. The TEM images presented in **Figure S6c** and **S6d** identify most Pt nanoparticles formed on the Cu_3P|S surface after 2-hour irradiation, indicating the photogenerated electrons in Cu_3P|S/CN are transferred to Cu_3P|S and used to reduce Pt^{4+} ions in solution [36]. This implies that the active reduction sites are mainly located on the Cu_3P|S surface while holes are kept on GL-C_3N_4, indicating a Z-scheme type composite. Recent computational calculations pointed out that the formation of chemical bonds at the interface can largely facilitate the charge carrier transfer and enhance the reducibility of electrons in the conduction band [22, 35]. We thus proposed the electron transfer mechanism for the Cu_3P|S/CN composite in **Figure 4d** based on these results. Under solar light, the E_F of GL-C_3N_4 and Cu_3P|S would shift to the same position in the Cu_3P|S/CN composite, where the P–N bonds act as an atomic-level interfacial pathway for the migration of photoexcited charge carriers. Specifically, the photoexcited electrons in the CB of GL-C_3N_4 quickly recombine with the holes in the VB of Cu_3P|S, leaving the electrons with stronger reduction ability in the CB of Cu_3P|S for the reaction with protons absorbed on the surface to generate H_2. Meanwhile, the holes with stronger oxidation ability remain in the VB of GL-C_3N_4 to achieve oxidation reaction with the sacrificial agent to complete the redox cycle. This leads to the promoted HER performance as a result of facilitated electron transfer as well as the suppressed recombination of charge carriers.

3.4. Kinetics of Cu_3P|S/GL-C_3N_4 Z-scheme system

To further validate our proposed mechanism and investigate carrier-migration kinetics at the P–N interface, the photoluminescent emission spectroscopy (PL) and time-resolved transient photoluminescence (TRPL) were employed. The PL spectra given in **Figure 5a** show that both GL-C_3N_4 and p-Cu_3P|S/CN exhibit a strong PL emission peak at *ca*. 460 nm which corresponds to the typical band gap excitation of GL-C_3N_4 [39]. Cu_3P|S/CN also shows a similar emission peak but

with considerably lower intensity, which can be explained by the formation of Z-scheme structure that prevent the charge-carrier recombination [21, 35]. This is supported by the TRPL measurements that can monitor the lifetime of charge carriers [47]. The TRPL spectra of GL-C_3N_4, p-Cu_3P|S/CN, and Cu_3P|S/CN are compared in **Figure 5b**, where Cu_3P|S/CN exhibits a faster decaying spectrum (average lifetime, τ_{ave} = 3.75 ns) than GL-C_3N_4 (τ_{ave} = 4.54 ns) and p-Cu_3P|S/CN (τ_{ave} = 4.83 ns). Fitting the TRPL spectra to the bi-exponential kinetic function yields two categories of charge carrier lifetimes, short lifetime (τ_1) and long lifetime (τ_2), and they are summarized in **Table S3**. The value of τ_1 is correlated with the radiation process (*i.e.*, the spontaneous recombination of charge carriers) and decreased by competition reaction, such as photocatalytic reduction reactions [48]. The τ_2 is associated with non-radiation energy transfer processes and a high percentage of τ_2 indicates the increased probability of charge carriers participating in photocatalytic reactions [49]. The τ_1 lifetimes of GL-C_3N_4 and Cu_3P|S/CN are 1.85 and 1.39 ns with the fractional contribution f_1 of 53.8 %, and 45.1 %, respectively. The smaller τ_1 and f_1 values of Cu_3P|S/CN suggest that the recombination rate of photogenerated charge carriers is effectively suppressed upon the formation of P–N chemical bonds [40, 50]. On the other hand, the τ_2 of Cu_3P|S/CN is shorter (5.71 ns) than that of GL-C_3N_4 (7.68 ns), while the fractional contribution f_2 of Cu_3P|S/CN has increased to 54.9 % from 46.2 % of GL-C_3N_4. This reveals a faster electron transfer and higher probability of charge carriers participating in photocatalytic reactions in Cu_3P|S/CN [28, 49]. Assuming that the observed decrease in lifetime arises from charge transfer from g-C_3N_4 to Cu_3P|S, the rate of electron transfer (k_{ET}) can be estimated using the equation $k_{ET} = 1/\tau_{ave}(Cu_3P|S/CN) - 1/\tau_{ave}(GL\text{-}C_3N_4)$ [26, 27]. A high k_{ET} value of 4.6×10^{11} s^{-1} obtained for Cu_3P|S/CN supports the positive effect of P–N bond that serves as an interfacial electron transfer channel. The improved migration efficiency is also supported by the apparently enhanced photocurrent density of Cu_3P|S/CN (0.17 μA cm^{-2}) compared with pristine GL-

C_3N_4 (0.08 μA cm^{-2}) at an applied potential of 0 V (**Figure 5c**).

3.5. Role of phosphosulfide structure in $Cu_3P|S/CN$

Despite the similar interfacial connection (XPS spectra, **Figure 3**) and the same band position (**Figure 4** and **S4**), $Cu_3P|S/CN$ shows a better photocatalytic HER activity than Cu_3P/CN, indicating that the PS structure also contributes to the enhanced photocatalytic performance. It was reported that the PS structure in $Cu_3P|S$ can minimize the Gibbs free energy (ΔG_{H*}) of hydrogen adsorption and considerably increase the number of active sites [16]. To confirm the role of PS structure, linear sweep voltammetry (LSV) and electrochemical impedance spectroscopy (EIS) were engaged using the catalyst-coated carbon fiber paper as the working electrode. As shown in **Figure 6a**, $Cu_3P|S/CN$ requires a lower overpotential (286 mV) than Cu_3P/CN (379 mV) to achieve the current density of 3 mA cm^{-2}, demonstrating the lowered energy barrier for driving hydrogen reduction reaction at the PS structure [36]. **Figure 6b** compares the Nyquist plots obtained from the EIS measurements at open circuit potential, in which $Cu_3P|S/CN$ exhibit much smaller charge transfer resistance than Cu_3P/CN. These clearly demonstrate the advantage of PS structure in promoting the conductivity and thus electron transfer rate [51].

4. Conclusion

In summary, $Cu_3P|S$ nanoplates were coupled with GL-C_3N_4 by an intimate interfacial contact to yield a highly efficient photocatalytic system for HER. The interface between $Cu_3P|S$ and GL-C_3N_4 was engineered to construct a Z-scheme composite with P–N chemical bonds that act as charge transfer pathway, effectively retarding the recombination rate and facilitating the separation of photogenerated charge carriers. Combined with abundant and highly active phosphosulfide structure, $Cu_3P|S/GL\text{-}C_3N_4$ exhibits an excellent photocatalytic HER rate of 8.78 mmol g^{-1} h^{-1} (20.22 mmol

g^{-1} h^{-1} with 0.5 wt.% Pt) and high durability, which outperforms most phosphide- and sulfide-assisted g-C_3N_4 composites. Our study offers useful insights to the rational interface engineering of photocatalysts for highly boosted performance.

Acknowledgement

X. Zhang and J. Yan contributed equally to this work. We gratefully acknowledge the financial supports from the Innovation and Technology Commission of Hong Kong and The Hong Kong Polytechnic University (1-BE0Y). J. Yan acknowledges the Postdoctoral Fellowships Scheme from the Hong Kong Polytechnic University (1-YW3J).

Supporting Information

An online version of Supplementary data including EDS elemental analysis, TEM and STEM images, XPS survey spectra, Tauc plots, Mott-Schottky plots associated with this article is available.

Conflict of Interest

The authors declare no conflict of interest.

Reference

[1] Y.J. Gao, X.B. Li, H.L. Wu, S.L. Meng, X.B. Fan, M.Y. Huang, Q. Guo, C.H. Tung, L.Z. Wu, Exceptional catalytic nature of quantum dots for photocatalytic hydrogen evolution without external cocatalysts, Adv. Funct. Mater., 28 (2018) 1801769.

[2] S. Yu, X.B. Fan, X. Wang, J. Li, Q. Zhang, A. Xia, S. Wei, L.Z. Wu, Y. Zhou, G.R. Patzke, Efficient photocatalytic hydrogen evolution with ligand engineered all-inorganic InP and InP/ZnS colloidal quantum dots, Nat. Commun., 9 (2018) 4009.

[3] B. Wang, S. He, L. Zhang, X. Huang, F. Gao, W. Feng, P. Liu, CdS nanorods decorated with inexpensive NiCd bimetallic nanoparticles as efficient photocatalysts for visible-light-driven photocatalytic hydrogen evolution, Appl. Catal. B Environ., 243 (2019) 229-235.

[4] W. Zhu, W. Gan, Z. Muhammad, C. Wang, C. Wu, H. Liu, D. Liu, K. Zhang, Q. He, H. Jiang, X. Zheng, Z. Sun, S. Chen, L. Song, Exfoliation of ultrathin $FePS_3$ layers as a promising electrocatalyst for the oxygen evolution reaction, Chem. Commun., 54 (2018) 4481-4484.

[5] D. Ma, J.-W. Shi, D. Sun, Y. Zou, L. Cheng, C. He, H. Wang, C. Niu, L. Wang, Au decorated hollow ZnO@ZnS heterostructure for enhanced photocatalytic hydrogen evolution: The insight into the roles of hollow channel and Au nanoparticles, Appl. Catal. B Environ., 244 (2019) 748-757.

[6] P.Y. Kuang, P.X. Zheng, Z.Q. Liu, J.L. Lei, H. Wu, N. Li, T.Y. Ma, Embedding Au quantum dots in rimous cadmium sulfide nanospheres for enhanced photocatalytic hydrogen evolution, Small, 12 (2016) 6735-6744.

[7] L. Yuan, C. Han, M.-Q. Yang, Y.-J. Xu, Photocatalytic water splitting for solar hydrogen generation: fundamentals and recent advancements, Int. Rev. Phys. Chem., 35 (2016) 1-36.

[8] V. Kumaravel, S. Mathew, J. Bartlett, S.C. Pillai, Photocatalytic hydrogen production using metal doped TiO_2: A review of recent advances, Appl. Catal. B Environ., 244 (2019) 1021-1064.

[9] W. Zhong, S. Shen, M. He, D. Wang, Z. Wang, Z. Lin, W. Tu, J. Yu, The pulsed laser-induced Schottky junction via in-situ forming Cd clusters on CdS surfaces toward efficient visible light-driven photocatalytic hydrogen evolution, Appl. Catal. B Environ., 258 (2019) 117967.

[10] J. Kibsgaard, T. Jaramillo, Molybdenum phosphosulfide: An active, acid-stable, earth-abundant catalyst for the hydrogen evolution reaction, Angew. Chem. Int. Ed., 53 (2014) 14433-14437.

[11] D.J. Li, J. Kang, H.J. Lee, D.S. Choi, S.H. Koo, B. Han, S.O. Kim, High activity hydrogen evolution catalysis by uniquely designed amorphous/metal interface of core-shell

phosphosulfide/N-doped CNTs, Adv. Energy Mater., 8 (2018) 1702806.

[12] W. Liu, E. Hu, H. Jiang, Y. Xiang, Z. Weng, M. Li, Q. Fan, X. Yu, E.I. Altman, H. Wang, A highly active and stable hydrogen evolution catalyst based on pyrite-structured cobalt phosphosulfide, Nat. Commun., 7 (2016) 10771.

[13] V. Veeramani, H.C. Yu, S.F. Hu, R.S. Liu, Highly efficient photoelectrochemical hydrogen generation reaction using tungsten phosphosulfide nanosheets, ACS Appl. Mater. Interfaces, 10 (2018) 17280-17286.

[14] J. Luo, H. Wang, G. Su, Y. Tang, H. Liu, F. Tian, D. Li, Self-supported nickel phosphosulphide nanosheets for highly efficient and stable overall water splitting, J. Mater. Chem. A, 5 (2017) 14865-14872.

[15] Z. Wu, X. Li, W. Liu, Y. Zhong, Q. Gan, X. Li, H. Wang, Materials chemistry of iron phosphosulfide nanoparticles: Synthesis, solid state chemistry, surface structure, and electrocatalysis for the hydrogen evolution reaction, ACS Catal., 7 (2017) 4026-4032.

[16] X. Zhang, K.-A. Min, W. Zheng, J. Hwang, B. Han, L.Y.S. Lee, Copper phosphosulfides as a highly active and stable photocatalyst for hydrogen evolution reaction, Appl. Catal. B Environ., 273 (2020) 118927.

[17] Z. Wang, C. Li, K. Domen, Recent developments in heterogeneous photocatalysts for solar-driven overall water splitting, Chem. Soc. Rev., 48 (2019) 2109-2125.

[18] Q. Xu, L. Zhang, B. Cheng, J. Fan, J. Yu, S-Scheme heterojunction photocatalyst, Chem, 6 (2020) 1543-1559.

[19] Y. Qu, X. Duan, Progress, challenge and perspective of heterogeneous photocatalysts, Chem. Soc. Rev., 42 (2013) 2568-2580.

[20] Q. Liu, J. Shen, X. Yang, T. Zhang, H. Tang, 3D reduced graphene oxide aerogel-mediated Z-scheme photocatalytic system for highly efficient solar-driven water oxidation and removal of antibiotics, Appl. Catal. B Environ., 232 (2018) 562-573.

[21] K. Wang, G. Zhang, J. Li, Y. Li, X. Wu, 0D/2D Z-Scheme heterojunctions of bismuth tantalate quantum dots/ultrathin g-C_3N_4 nanosheets for highly efficient visible light photocatalytic degradation of antibiotics, ACS Appl. Mater. Interfaces, 9 (2017) 43704-43715.

[22] Y.-J. Yuan, Z.-K. Shen, S. Song, J. Guan, L. Bao, L. Pei, Y. Su, S. Wu, W. Bai, Z.-T. Yu, Z. Ji, Z. Zou, Co–P bonds as atomic-level charge transfer channel to boost photocatalytic H_2 production of Co_2P/Black phosphorus nanosheets photocatalyst, ACS Catal., 9 (2019) 7801-

7807.

[23] M. Ou, W. Tu, S. Yin, W. Xing, S. Wu, H. Wang, S. Wan, Q. Zhong, R. Xu, Amino-assisted anchoring of $CsPbBr_3$ perovskite quantum dots on porous g-C_3N_4 for enhanced photocatalytic CO_2 reduction, Angew. Chem. Int. Ed., 57 (2018) 13570-13574.

[24] J. Yan, Z. Chen, H. Ji, Z. Liu, X. Wang, Y. Xu, X. She, L. Huang, L. Xu, H. Xu, H. Li, Construction of a 2D graphene-Like MoS_2/C_3N_4 heterojunction with enhanced visible-light photocatalytic activity and photoelectrochemical activity, Chem. Eur. J., 22 (2016) 4764-4773.

[25] H. Yu, R. Shi, Y. Zhao, T. Bian, Y. Zhao, C. Zhou, G.I.N. Waterhouse, L.Z. Wu, C.H. Tung, T. Zhang, Alkali-assisted synthesis of nitrogen deficient graphitic carbon nitride with tunable band structures for efficient visible-light-driven hydrogen evolution, Adv. Mater., 29 (2017) 1605148.

[26] I. Robel, V. Subramanian, M. Kuno, P.V. Kamat, Quantum dot solar cells. Harvesting light energy with CdSe nanocrystals molecularly linked to mesoscopic TiO_2 films, J. Am. Chem. Soc., 128 (2006) 2385-2393.

[27] B.C. Fitzmorris, G.K. Larsen, D.A. Wheeler, Y. Zhao, J.Z. Zhang, Ultrafast charge transferdynamics in polycrystalline CdSe/TiO_2 nanorods prepared by oblique angle codeposition, J. Phys. Chem. C, 116 (2012) 5033-5041.

[28] F. Liu, R. Shi, Z. Wang, Y. Weng, C.M. Che, Y. Chen, Direct Z-scheme hetero-phase junction of Black/Red phosphorus for photocatalytic water splitting, Angew. Chem. Int. Ed., 58 (2019) 11791-11795.

[29] G. Manna, R. Bose, N. Pradhan, Semiconducting and plasmonic copper phosphide platelets, Angew. Chemie., 125 (2013) 6894-6898.

[30] W. Wang, X. Zhao, Y. Cao, Z. Yan, R. Zhu, Y. Tao, X. Chen, D. Zhang, G. Li, D. Phillips, Copper phosphide-enhanced lower charge trapping occurrence in graphitic-C_3N_4 for efficient noble-metal-free photocatalytic H_2 evolution, ACS Appl. Mater. Interfaces, 11 (2019) 16527.

[31] J. Yan, Y. Fan, J. Lian, Y. Zhao, Y. Xu, J. Gu, Y. Song, H. Xu, H. Li, Kinetics and mechanism of enhanced photocatalytic activity employing ZnS nanospheres/graphene-like C_3N_4, Mol. Catal., 438 (2017) 103-112.

[32] W. Wang, T. An, G. Li, D. Xia, H. Zhao, J.C. Yu, P.K. Wong, Earth-abundant Ni_2P/g-C_3N_4 lamellar nanohydrids for enhanced photocatalytic hydrogen evolution and bacterial inactivation under visible light irradiation, Appl. Catal. B Environ., 217 (2017) 570-580.

[33] X. Wang, X. Tian, Y. Sun, J. Zhu, F.T. Li, H. Mu, J. Zhao, Enhanced schottky effect of a 2D-2D

CoP/g-C_3N_4 interface for boosting photocatalytic H_2 evolution, Nanoscale, 10 (2018) 12315-12321.

[34] M. Pi, T. Yang, S. Wang, S. Chen, One-pot synthesis of in situ carbon-decorated Cu_3P particles with enhanced electrocatalytic hydrogen evolution performance, J. Mater. Res., 33 (2017) 546-555.

[35] F. Zhang, J. Zhang, J. Li, X. Jin, Y. Li, M. Wu, X. Kang, T. Hu, X. Wang, W. Ren, G. Zhang, Modulating charge transfer dynamics for g-C_3N_4 through a dimension and interface engineered transition metal phosphide Co-catalyst for efficient visible-light photocatalytic hydrogen generation, J. Mater. Chem. A, 7 (2019) 6939-6945.

[36] S. Hua, D. Qu, L. An, W. Jiang, Y. Wen, X. Wang, Z. Sun, Highly efficient p-type Cu_3P/n-type g-C_3N_4 photocatalyst through Z-scheme charge transfer route, Appl. Catal. B Environ., 240 (2019) 253-261.

[37] Tarachand, S. Hussain, N.P. Lalla, Y.K. Kuo, A. Lakhani, V.G. Sathe, U. Deshpande, G.S. Okram, Thermoelectric properties of Ag-doped CuS nanocomposites synthesized by a facile polyol method, Phys. Chem. Chem. Phys., 20 (2018) 5926-5935.

[38] M. Luo, Q. Yang, K. Liu, H. Cao, H. Yan, Boosting photocatalytic H_2 evolution on g-C_3N_4 by modifying covalent organic frameworks (COFs), Chem. Commun., 55 (2019) 5829-5832.

[39] R. Shen, J. Xie, X. Lu, X. Chen, X. Li, Bifunctional Cu_3P decorated g-C_3N_4 nanosheets as a highly active and robust visible-light photocatalyst for H_2 production, ACS Sustainable Chem. Eng., 6 (2018) 4026-4036.

[40] X. Zhu, H. Ji, J. Yi, J. Yang, X. She, P. Ding, L. Li, J. Deng, J. Qian, H. Xu, H. Li, A specifically exposed cobalt oxide/carbon nitride 2D heterostructure for carbon dioxide photoreduction, Ind. Eng. Chem. Res., 57 (2018) 17394-17400.

[41] S. Trasatti, The absolute electrode potential: An explanatory note, Pure Appl. Chem., 58 (1986) 955-966.

[42] Z. Hong, B. Shen, Y. Chen, B. Lin, B. Gao, Enhancement of photocatalytic H_2 evolution over nitrogen-deficient graphitic carbon nitride, J. Mater. Chem. A, 1 (2013) 11754.

[43] X. Yue, S. Yi, R. Wang, Z. Zhang, S. Qiu, A novel and highly efficient earth-abundant Cu_3P with TiO_2 "P-N" heterojunction nanophotocatalyst for hydrogen evolution from water, Nanoscale, 8 (2016) 17516-17523.

[44] H. Wang, L. Zhang, Z. Chen, J. Hu, S. Li, Z. Wang, J. Liu, X. Wang, Semiconductor

heterojunction photocatalysts: design, construction, and photocatalytic performances, Chem. Soc. Rev., 43 (2014) 5234-5244.

[45] J. Yang, J. Hao, S. Xu, Q. Wang, J. Dai, A. Zhang, X. Pang, $InVO_4$/beta-$AgVO_3$ nanocomposite as a direct Z-scheme photocatalyst toward efficient and selective visible-light-driven CO_2 reduction, ACS Appl. Mater. Interfaces, 11 (2019) 32025-32037.

[46] J. Fu, Q. Xu, J. Low, C. Jiang, J. Yu, Ultrathin 2D/2D WO_3/g-C_3N_4 step-scheme H_2-production photocatalyst, Appl. Catal. B Environ., 243 (2019) 556-565.

[47] K. Das, S.N. Sharma, M. Kumar, S. De, Morphology dependent luminescence properties of Co doped TiO_2 nanostructures, J. Phys. Chem. C, 113 (2009) 14783-14792.

[48] P. Xia, S. Cao, B. Zhu, M. Liu, M. Shi, J. Yu, Y. Zhang, Designing a 0D/2D S-scheme heterojunction over polymeric carbon nitride for visible-light photocatalytic inactivation of bacteria, Angew. Chem. Int. Ed., 59 (2020) 5218-5225.

[49] P. Niu, G. Liu, H.-M. Cheng, Nitrogen vacancy-promoted photocatalytic activity of graphitic carbon nitride, J. Phys. Chem. C, 116 (2012) 11013-11018.

[50] W. Liu, L. Cao, W. Cheng, Y. Cao, X. Liu, W. Zhang, X. Mou, L. Jin, X. Zheng, W. Che, Q. Liu, T. Yao, S. Wei, Single-site active cobalt-based photocatalyst with a long carrier lifetime for spontaneous overall water splitting, Angew. Chem. Int. Ed., 56 (2017) 9312-9317.

[51] S. Wang, B. Zhu, M. Liu, L. Zhang, J. Yu, M. Zhou, Direct Z-scheme ZnO/CdS hierarchical photocatalyst for enhanced photocatalytic H_2-production activity, Appl. Catal. B Environ., 243 (2019) 19-26.

Figures

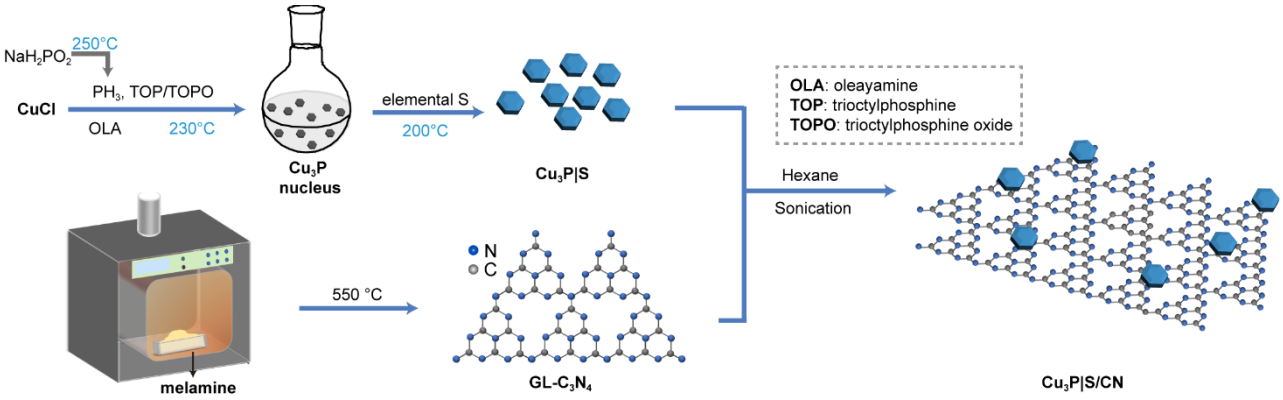

Scheme 1. Synthetic route of $Cu_3P|S/GL\text{-}C_3N_4$ nanocomposite.

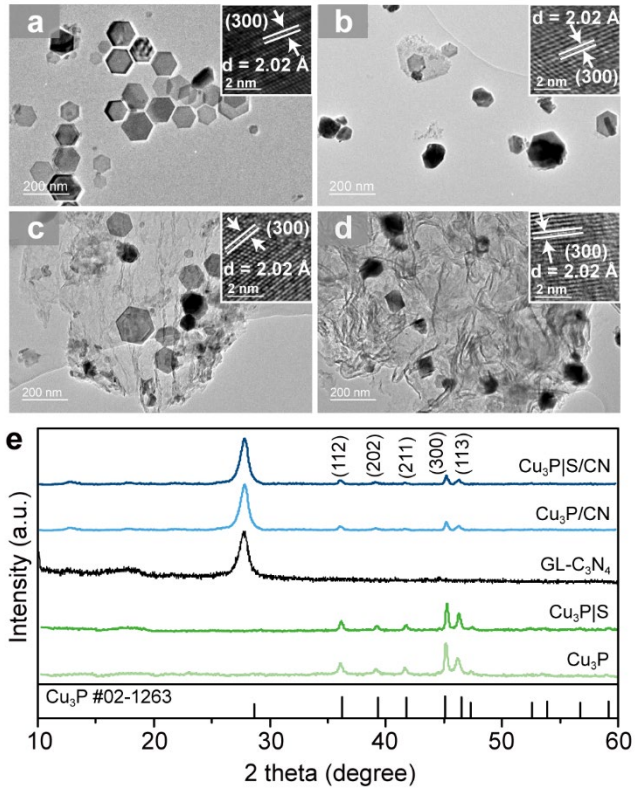

Figure 1. TEM images of (a) Cu_3P, (b) $Cu_3P|S$, (c) Cu_3P/CN, and (d) $Cu_3P|S/CN$. Insets in (a-d) are the corresponding HRTEM images. (e) XRD patterns of Cu_3P, $Cu_3P|S$, $GL\text{-}C_3N_4$, Cu_3P/CN, and $Cu_3P|S/CN$.

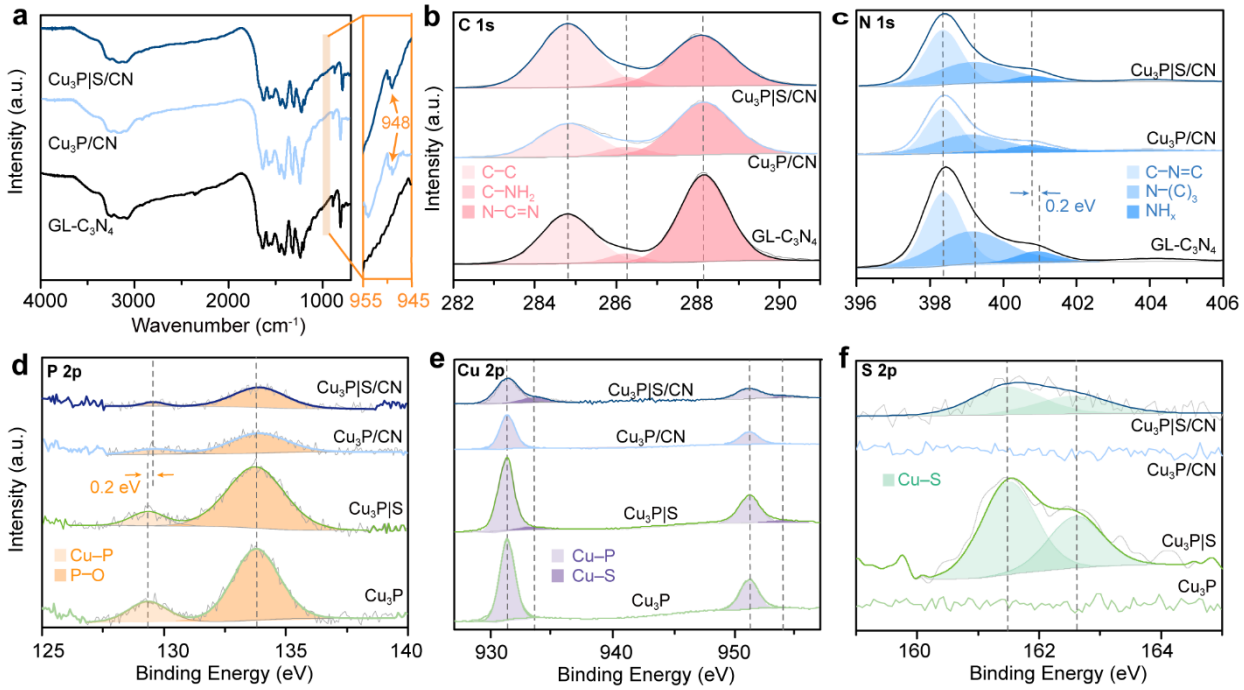

Figure 2. (a) FTIR and (b-f) XPS spectra of GL-C_3N_4, Cu_3P/CN, and Cu_3P|S/CN. (b) C 1s, (c) N 1s, (d) P 2p, (e) Cu 2p, and (f) S 2p region.

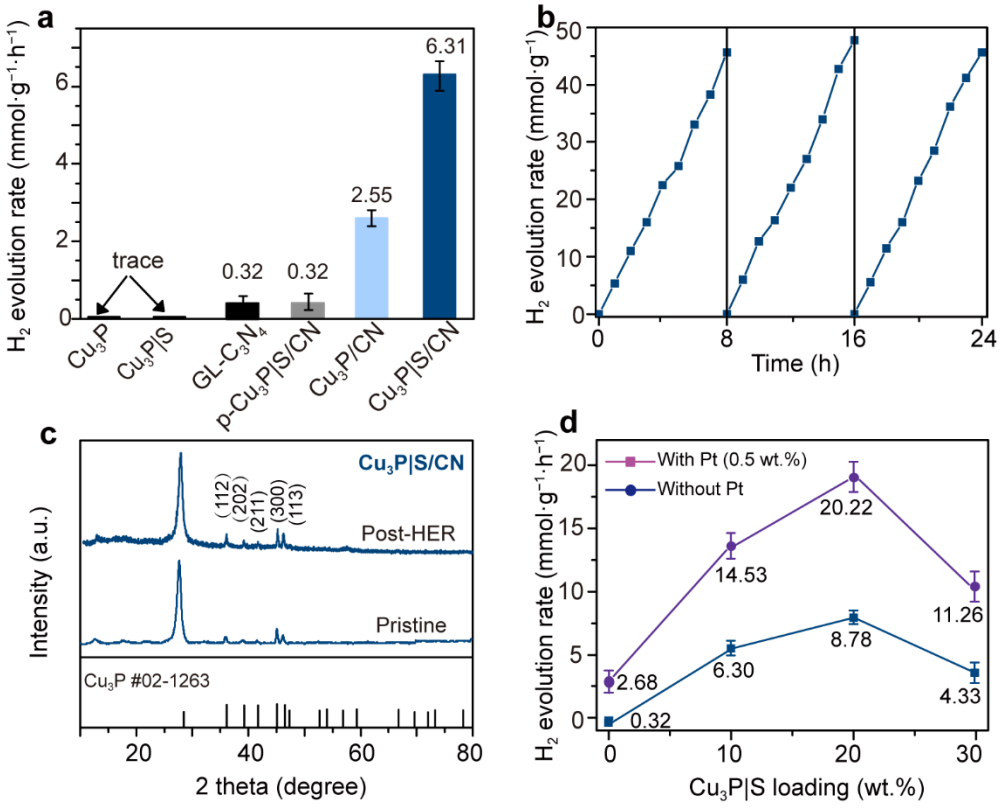

Figure 3. (a) H_2 generation rate of pristine Cu_3P, $Cu_3P|S$, GL-C_3N_4, p-$Cu_3P|S/CN$, Cu_3P/CN, and $Cu_3P|S/CN$ composites, (b)long-term photocatalytic HER rate of $Cu_3P|S/CN$, (c) XRD pattern of $Cu_3P|S/CN$ composite after photocatalytic reaction, and (d) HER rate of $Cu_3P|S/GL\text{-}C_3N_4$ composites with various $Cu_3P|S$ loading amount.

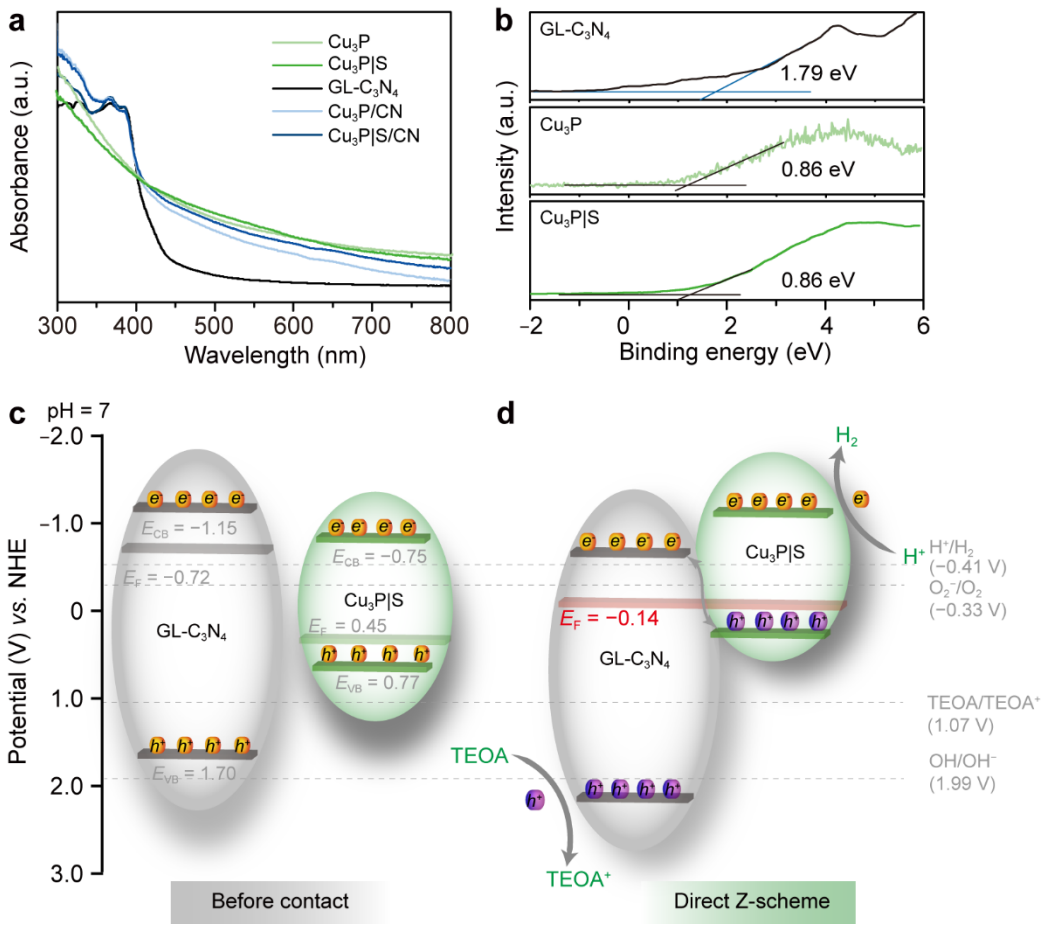

Figure 4. (a) UV-Vis DRS spectra of Cu_3P, $Cu_3P|S$, GL-C_3N_4, Cu_3P/CN, and $Cu_3P|S$/CN. (b) VB-XPS spectra of GL-C_3N_4, Cu_3P, and $Cu_3P|S$. (c) Schematic diagram of the electronic structures of $Cu_3P|S$ and GL-C_3N_4 before composite formation and (d) the proposed Z-scheme photocatalytic system of $Cu_3P|S$/CN composite.

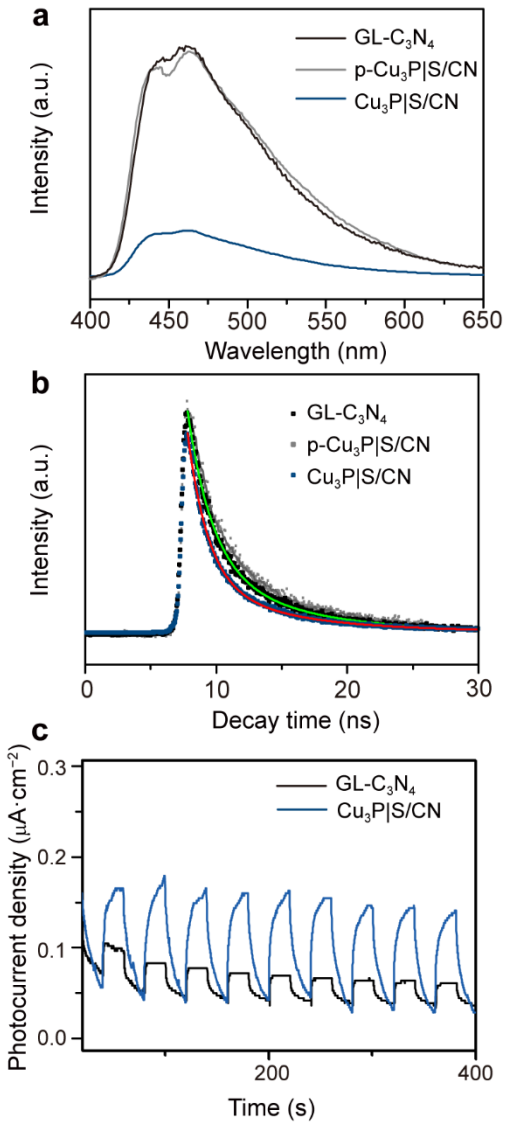

Figure 5. (a) Photoluminescence (PL) and (b) time-resolved photoluminescence (TRPL) spectra of GL-C_3N_4, p-Cu_3P|S/CN, and Cu_3P|S/CN of GL-C_3N_4, Cu_3P/CN, and Cu_3P|S/CN. (c) Photocurrent response of GL-C_3N_4 and Cu_3P|S/CN.

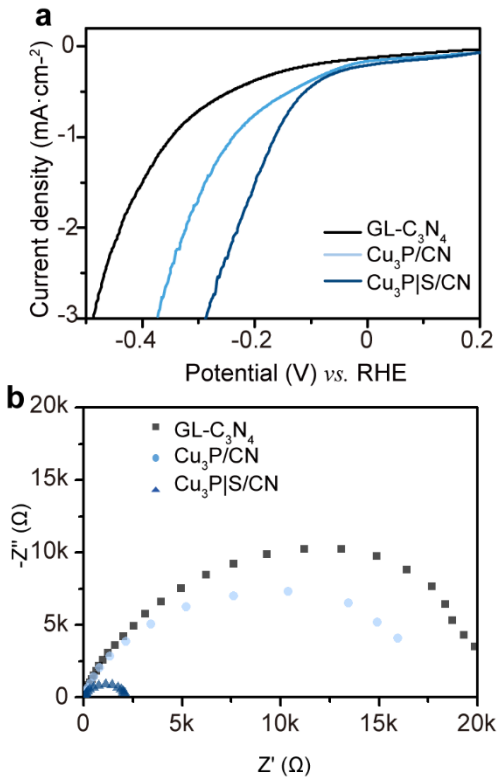

Figure 6. (a) LSV curves and (b) EIS spectra of GL-C_3N_4, Cu_3P|S/CN, and Cu_3P|S/CN.